

A CENSUS OF THE HIGH-DENSITY MOLECULAR GAS IN M82

B.J. NAYLOR¹, C.M. BRADFORD¹, J.E. AGUIRRE², J.J. BOCK¹, L. EARLE³, J. GLENN³, H. INAMI⁴, J. KAMENETZKY³, P.R. MALONEY³, H. MATSUHARA⁴, H.T. NGUYEN¹, J. ZMUIDZINAS¹*submitted to the Astrophysical Journal*

ABSTRACT

We present a three-pointing study of the molecular gas in the starburst nucleus of M82 based on 190–307 GHz spectra obtained with Z-Spec at the Caltech Submillimeter Observatory. We measure intensities or upper-limits for 20 transitions, including several new detections of CS, HNC, C₂H, H₂CO and CH₃CCH lines. We combine our measurements with previously-published measurements at other frequencies for HCN, HNC, CS, C³⁴S, and HCO⁺ in a multi-species likelihood analysis constraining gas mass, density and temperature, and the species’ relative abundances. We find some $1.7\text{--}2.7 \times 10^8 M_{\odot}$ of gas with n_{H_2} between $1\text{--}6 \times 10^4 \text{ cm}^{-3}$ and $T > 50 \text{ K}$. While the mass and temperature are comparable to values inferred from mid- J CO transitions, the thermal pressure is a factor of 10–20 greater. The molecular ISM is largely fragmented and is subject to UV irradiation from the star clusters. It is also likely subject to cosmic rays and mechanical energy input from the supernovae, and is warmer on average than the molecular gas in the massive star formation regions in the Milky Way. The typical conditions in the dense gas in M82’s central kpc appear unfavorable for further star formation; if any appreciable stellar populations are currently forming, they are likely biased against low mass stars, producing a top-heavy IMF.

Subject headings: galaxies: abundances — galaxies: individual (M82) — galaxies: ISM — galaxies: starburst — instrumentation: spectrographs — techniques: spectroscopic

1. INTRODUCTION

Studies of molecular gas - the actively star-forming part of the interstellar medium - in other galaxies have been carried out most extensively in the low-lying rotational transitions of the CO molecule. Due to its high abundance relative to molecular hydrogen and its favorable energy level spacing as compared to typical molecular cloud temperatures, CO produces the brightest lines in the millimeter-wavelength portion of the spectrum.

However, while these lines trace the bulk of the molecular gas, the small dipole moment of CO results in modest critical densities for these lines, $\sim 10^3 - 10^4 \text{ cm}^{-3}$, and thus they do not strongly discriminate between high-density star-forming cores and more diffuse gas. High-dipole-moment molecules such as HCN and CS have critical densities and radiative rates that are 100–1000 times larger than CO. Despite their much smaller abundances, these species can be used to probe the dense ($10^4 - 10^7 \text{ cm}^{-3}$) cloud cores believed to be associated with star formation. Early measurement of HCN and CS in the Galaxy (Morris et al. 1974; Turner et al. 1973) and in external galaxies (Henkel et al. 1988; Solomon et al. 1992) showed that their intensities are well-correlated with the total far-IR flux. More recently, HCN $J=1 \rightarrow 0$ luminosity has been shown to be directly proportional to far-IR luminosity (a proxy for star formation rate) in a sample of ~ 100 galaxies of various types (Gao & Solomon 2004b,a), as well as individual star-formation sites in the Galaxy (Wu et al. 2005).

Insofar as HCN $J=1 \rightarrow 0$ measures dense gas mass, the $L_{\text{FIR}} / \text{HCN}$ correlation across 7–8 orders of magnitude in luminosity implies a scale-independent relationship between dense gas mass and star formation rate. An accurate assessment of the physical conditions in the HCN-emitting gas as well as the mass scaling ($M_{\text{H}_2}/I_{\text{HCN}}$) is thus of universal interest for theoretical star formation studies. Is the HCN-emitting gas simply a bi-product of star formation, perhaps formed in shocks or outflows and not participating in the formation of new stars, or is some of it the very material from which new stars form? Such an assessment is best made with multiple transitions of HCN and by including transitions from other high-dipole-moment molecules where available.

To assess the average properties of the dense gas on the scale of a nuclear starburst, we have observed the nucleus of the M82 in a suite of millimeter-wave transitions of high-dipole moment species. The brightest infrared galaxy in the sky due to its proximity (3.9 Mpc: Sakai & Madore 1999), M82 radiates an infrared luminosity ($L = 5.9 \times 10^{10} L_{\odot}$: Sanders et al. 2003), exceeding that of the Galaxy, from a region that is only about 450 pc in radius (e.g., Leeuw & Robson 2009). Because of this concentration of star-forming activity, M82 has been dubbed the prototypical starburst galaxy, which makes it a particularly interesting laboratory for the study of star formation. It has been suggested for over 30 years that the stellar IMF in M82 (and presumably other starburst nuclei) is biased against low-mass stars relative to the local IMF (Rieke et al. 1980, 1993; Förster Schreiber et al. 2003), but this has been debated (see e.g. Satyapal et al. 1997; Colbert et al. 1999). If the IMF is indeed low-mass deficient, a plausible line of inquiry is the initial conditions of star formation – the temperature and density of the dense molecular cloud cores.

¹ Jet Propulsion Laboratory, California Institute of Technology, Pasadena, CA, 91109

² University of Pennsylvania, Philadelphia, PA 19104

³ Dept. of Astrophysical and Planetary Sciences, University of Colorado, 389-UCB, Boulder, CO 80309

⁴ ISAS / JAXA, Sagami-hara, Japan

We have obtained full 190–307 GHz spectra with the Z-Spec 1-mm grating spectrometer, which accesses the $J = 3 \rightarrow 2$ transitions of HCN, HCO^+ , and HNC and $J = 4 \rightarrow 3$, $J = 5 \rightarrow 4$, and $J = 6 \rightarrow 5$ transitions of CS, with a uniform calibration. Our study benefits from the prior observations of $J = 1 \rightarrow 0$ transitions of HCN, HNC, HCO^+ (Nguyen-Q-Rieu et al. 1989; Huettemeister et al. 1995), as well as $J = 4 \rightarrow 3$ transitions of HCN, HCO^+ (Seaquist & Frayer 2000). These data are combined with our observations to generate the first comprehensive multi-species excitation and radiative transfer model for the dense gas in this source. Of course, since M82 is also well-studied in multiple CO transitions (Wild et al. 1992; Mao et al. 2000; Ward et al. 2003; Weiß et al. 2005; Seaquist et al. 2006; Panuzzo et al. 2010) as well as in the mid- and far-IR atomic gas tracers (Förster Schreiber et al. 2003; Colbert et al. 1999), we have the opportunity to put the dense gas into context with the other ISM components, as well as the general properties of this prototypical nuclear starburst.

2. OBSERVATIONS

Z-Spec is the first grating spectrometer for the millimeter band; it covers the full 190–307 GHz range instantaneously, dispersing this band to an array of 160 bolometers. More information can be found in Glenn et al. (2007), Bradford et al. (2009) and the SPIE articles: Naylor et al. (2003); Bradford et al. (2004); Earle et al. (2006). The instrument operates at the Nasmyth focus of the Caltech Submillimeter Observatory (CSO) atop Mauna Kea. While the instrument is $1/f$ stable down to ~ 100 mHz, we use a chop and nod mode to avoid the atmospheric fluctuations, which become important relative to the fundamental noise sources at ~ 0.3 –1 Hz, depending on the atmospheric conditions. For the M82 observations the chop frequency was 1.6 Hz, the throw was $90''$ in azimuth, and the nod interval was 20 seconds. Three pointings along M82’s major axis were observed on 2009 January 5 as summarized in Figure 1 and Table 1. The M82 spectra are calibrated using Mars, with an interpolation scheme using bolometer operating voltages as a measure of response (Earle 2008; Bradford et al. 2009). The data were reduced with standard demodulation and differencing appropriate for the chop and nod observing mode and Uranus is used as a spectral flat-fielder. We expect the channel-to-channel calibration uncertainties to be less than 10% except at the lowest frequencies which are extremely sensitive to the wing of the 186 GHz atmospheric water line.

3. RESULTS

Spectra for the NE, CEN and SW pointings are shown in Figure 2. The general features agree with previous measurements of the 1.2-mm continuum and CO $J = 2 \rightarrow 1$, such as those in Figure 1.

3.1. Continuum Fluxes and Fits

The continuum flux in the Z-Spec band is due to a combination of the thermal dust emission which dominates at higher frequencies and the free-free emission from [H II] region electrons which dominates at lower frequencies. The dust emission is parameterized as

Table 1
M82 Observed Positions

Pointing	α offset (arcsec)	δ offset (arcsec)	Int. Time (min)	Sensitivity (Jy s ^{1/2})
NE	+12.2	+3.3	60.2	1.3
CEN	+2.7	−0.5	68.6	1.4
SW	−6.1	−3.8	60.1	1.2

Note. — The R. A. and Dec. offsets are relative to $\alpha_{J2000.0} = 9^{\text{h}}55^{\text{m}}51.9^{\text{s}}$, $\delta_{J2000.0} = 69^{\circ}40'47.14''$. The integration time is the total demodulated time; the on-source time is half the listed values. The quoted sensitivity is the median value of channel errors multiplied by the square root of the integration time and does not represent the ultimate sensitivity of the instrument; Z-Spec’s sensitivity to spectral lines and to fainter sources is better by at least a factor of two. The optical depth during these observations was $\tau_{225\text{GHz}} = 0.08 - 0.1$.

$$F_{\text{T}}(\nu) = \Omega B_{\nu}(T) \left\{ 1 - \exp \left[- \left(\frac{\lambda_0}{\lambda} \right)^{\beta} \right] \right\}, \quad (1)$$

where $B_{\nu}(T) = (2h\nu^3/c^2)/(\exp[h\nu/kT] - 1)$ is the Planck function. Hughes et al. (1994) fit a collection of observations from 3.3 mm to 40 μm and derive $\Omega = 1.34 \times 10^{-8}$ sr, $T = 48.1$ K, $\beta = 1.3$ and $\lambda_0 = 7.9$ microns for the thermal dust. The free-free emission is given by a simple power law,

$$F_{\text{ff}}(\nu) = F_0 \left(\frac{\nu}{\nu_0} \right)^{-0.1}, \quad (2)$$

where F_0 is the free-free flux at ν_0 . Analysis of a map of M82 at 92 GHz found that the emission at that frequency is dominated by free-free emission – Carlstrom & Kronberg (1991) calculate the free-free flux density $F_{\text{ff}}(92 \text{ GHz}) = 0.5 \pm 0.1$ Jy. In the Z-Spec band, the free-free emission accounts for roughly one quarter of the total continuum flux, but that is significant enough that a dust-only fit to our spectra does not match the continuum level. Instead, we model the continuum flux we observe to be a beam-scaled fraction of the total continuum emission of the galaxy,

$$F(\nu) = A \left(\frac{\nu}{240 \text{ GHz}} \right)^{B-2} [F_{\text{T}}(\nu) + F_{\text{ff}}(\nu)]. \quad (3)$$

This model assumes that the free-free and thermal continuum emission have the same spatial distribution, which is reasonable given our coarse spatial resolution. It also accounts for the spectral dependence caused by the spatial distribution. If M82 completely filled our beam at all frequencies, we would expect $B = 0$, while $B = 2$ would be the prediction for a point source. We find that $B = 1$ is the best fit value for all three pointings (see Table 2), which makes sense given that M82 is observed edge on and is thus roughly point-like in one dimension and beam-filling in the other, relative to our $30''$ beam. The continuum fraction seen in the three pointings is consistent with the 1.2 mm continuum distribution shown in Thuma et al. (2000). The peak of the 1.2 mm continuum is at the center of the SW pointing which has the largest continuum fraction and smallest beam-scaling exponent of the three pointings. The continuum peak is within the CEN pointing and its fraction is almost equal to the SW

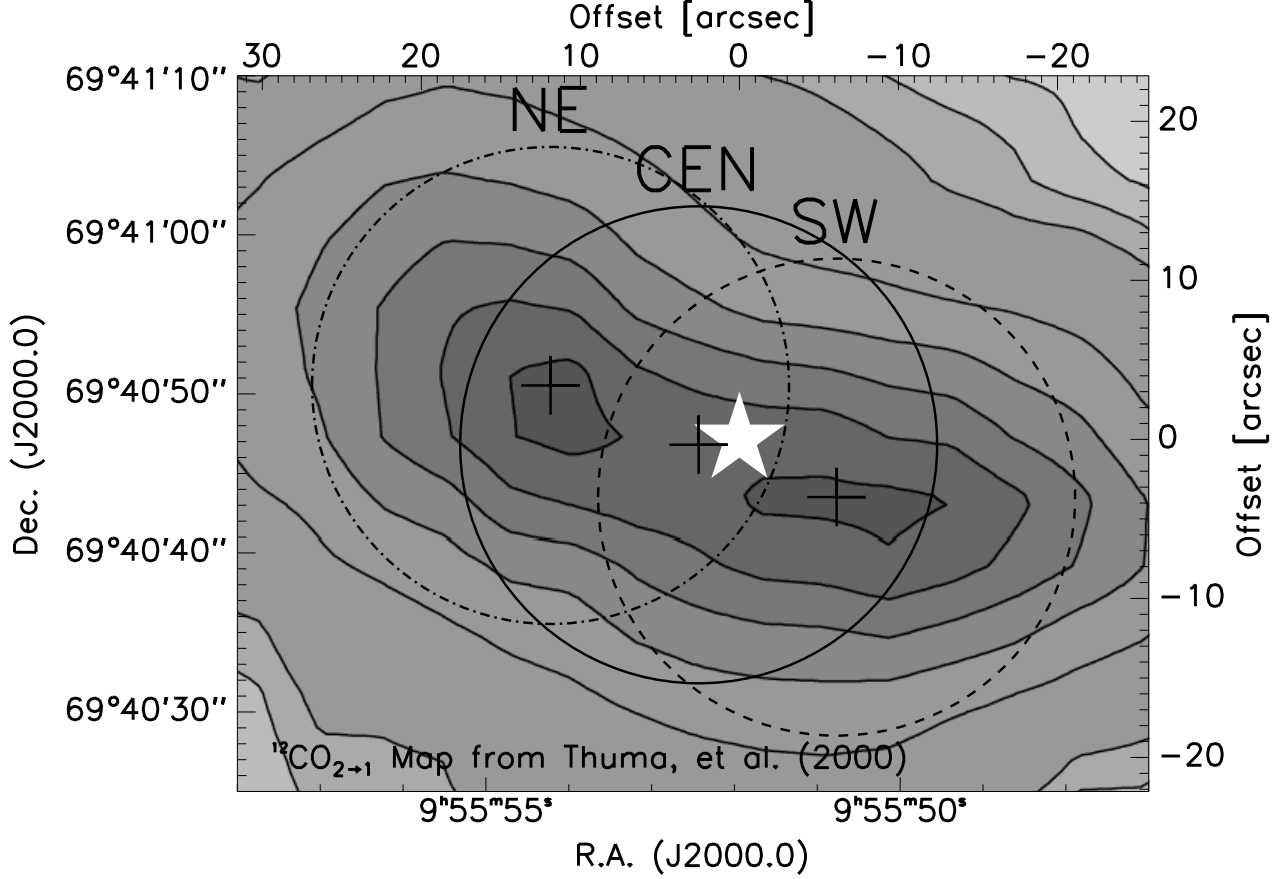


Figure 1. Pointings toward M82. Z-Spec’s 30'' beam (FWHM at 250 GHz) is plotted over the single-dish measurements of the ^{12}CO 2-1 map from Thuma et al. (2000). The white star marks the $2.2\ \mu\text{m}$ peak at $\alpha_{J2000.0} = 9^{\text{h}}55^{\text{m}}51.9^{\text{s}}$, $\delta_{J2000.0} = 69^{\circ}40'47.14''$ which is the adopted center for the observations. The offsets relative to the center and integration times are given in Table 1. All three pointings use a 90'' symmetric azimuthal chop throw.

Table 2
Continuum Fit Results

Pointing	Continuum Fit		Reduced χ^2
	A	B	
NE	0.318 ± 0.001	1.03 ± 0.03	2.4
CEN	0.413 ± 0.001	1.05 ± 0.02	3.2
SW	0.425 ± 0.001	0.99 ± 0.02	3.7

Note. — The continuum fit columns give the coupling fraction (A) and beam scaling exponent (B) of the fit described in Section 3.1 and defined in equation 3. The reduced χ^2 values are for the line and continuum fits and are calculated based solely on statistical errors and do not include errors due to calibration. The fits use all data points except the lowest five channels in each spectrum and have 132 degrees of freedom.

but with a higher index. The NE pointing’s continuum fraction is the smallest because it is off the peak.

3.2. Spectral Line Fitting Results

The channel-to-channel spacing in Z-Spec is 500–1300 MHz, corresponding to 700–1200 km s^{-1} , thus the instrument does not resolve the line profiles in M82. Nevertheless, it is possible to fit integrated intensities and center frequencies by comparison with the instrumental

response for each bolometer, carefully measured in the laboratory with a long-path Fourier-transform spectrometer. Each spectral line (indexed by j) is modeled as a Gaussian profile of center frequency ν_j , amplitude A_j , and FWHM $\delta\nu_j$. The sum of these line profiles plus the continuum is multiplied by the (normalized) measured spectral profile of each channel used in the fitting (indexed by i) $f_i(\nu)$ and integrated over the range of the measured profiles: 180–320 GHz. This process creates a model Z-Spec spectrum, which can be compared to the observed spectrum. The input line frequencies and amplitudes are then varied to arrive at a least-squares fit, using statistical $(1/\sigma_i^2)$ weighting. The frequencies of the known lines are fixed in the fitting, modulo a common redshift, so that the fit determines the redshift but not the line frequencies. In practice for local-Universe galaxies, the ^{12}CO transition dominates the redshift determination. With this method, we obtain accurate centroid measurements of line features that did not have an obvious identification. The fitted line intensities are given in Table 3 using the adopted $\Delta v = 250\ \text{km s}^{-1}$ for all lines in the three pointings; reducing the FWHM to 100 km s^{-1} produces nearly identical integrated intensities and fit quality. We comment here on our spectral line measurements and how they compare to those found in

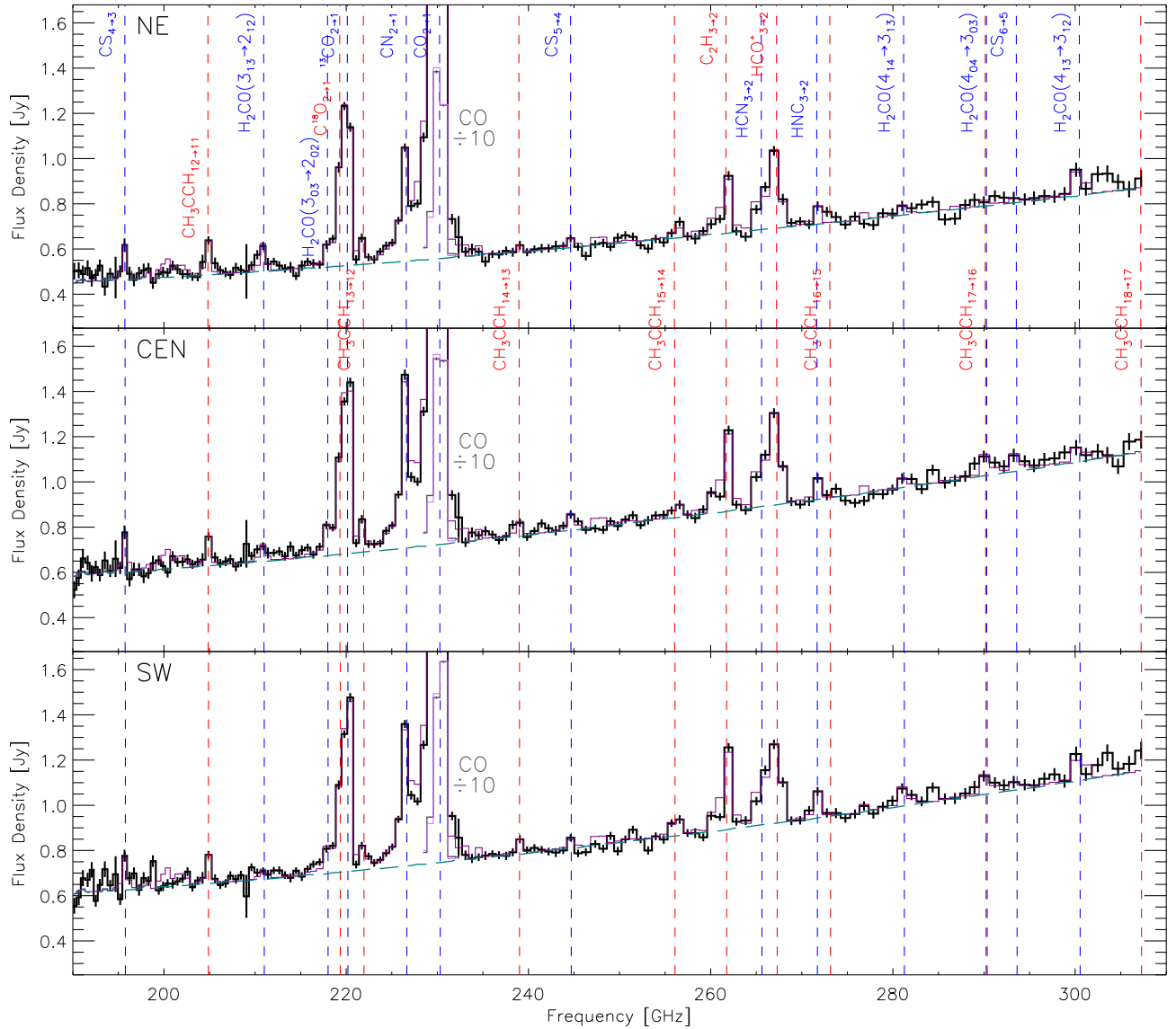


Figure 2. Z-Spec 190–307 GHz spectra toward three positions in the nucleus of M82: NE at the top, CEN in the middle and SW on the bottom. The black histogram with error bars are the calibrated measurements and the purple histogram is the spectral fit, including both continuum and 20 fitted lines. The fitted continuum is also plotted in dashed dark green and the fitted lines are marked with vertical blue and red dashed lines. The dominant CO $J=2 \rightarrow 1$ line is shown in gray on the plot, scaled down by a factor of ten; the fit to the CO line, also scaled down, is shown in lavender. The $\text{CH}_3\text{CCH } J=16 \rightarrow 15$ transitions and above are shown for reference but are not included in the fit. We have identified all three sigma or greater spectral-line features that appear in all three pointings. Nonetheless, there is additional structure in the spectra probably due to a multitude of blended, weak lines which Z-spec cannot individually identify. The results from the fits are given in in Tables 2 and 3.

the literature.

3.2.1. CO and its Isotopologues

The CO, ^{13}CO and $\text{C}^{18}\text{O } J=2 \rightarrow 1$ transitions have been extensively studied and mapped by previous experiments (Mao et al. 2000; Weiß et al. 2001); however, direct comparison with published intensities is limited by beam size mismatch. Wild et al. (1992) quote integrated main-beam intensities nearly twice what we measure in a $13''$ beam for the CO $J=2 \rightarrow 1$ transition, implying

a beamsize (θ) scaling of $I \propto \theta^{-0.8}$ whereas the main species intensities given in Mao et al. (2000) in a $22''$ beam indicate a beam scaling exponent of -1.2 to -1.5 . The maps in (Thuma et al. 2000) show that the CO emission is more extended than the continuum emission which would indicate the exponent should be slightly less than unity. The isotopologues ^{13}CO and C^{18}O have been measured in Mao et al. (2000) and Wild et al. (1992), respectively, and though they indicate different beam scaling exponents as they did for the main species, they both

Table 3
M82 Line Fit Results

Species & Transition	Rest Freq. (GHz)	E_{upper} (K)	Beam Size (arcsec)	Integrated Line Intensity (K km s ⁻¹)		
				NE	CEN	SW
CO $J=2 \rightarrow 1$	230.538	16.6	32	423.9 \pm 3.0	460.0 \pm 3.2	452.5 \pm 3.3
¹³ CO $J=2 \rightarrow 1$	220.399	15.9	34	29.4 \pm 0.7	31.7 \pm 0.7	30.2 \pm 0.7
C ¹⁸ O $J=2 \rightarrow 1$	219.560	15.8	34	8.6 \pm 0.7	7.9 \pm 0.7	7.8 \pm 0.7
CN $J=2 \rightarrow 1$	226.875	16.3	33	14.3 \pm 0.6	23.3 \pm 0.8	19.9 \pm 0.6
CS $J=4 \rightarrow 3$	195.954	23.5	37	4.3 \pm 0.8	4.4 \pm 0.8	4.1 \pm 0.7
CS $J=5 \rightarrow 4$	244.936	35.3	31	< 1.6 [1.2]	2.3 \pm 0.5	< 1.5 [1.1]
CS $J=6 \rightarrow 5$	293.912	49.4	26	< 3.1 [0.8]	< 3.3 [3.0]	< 3.1 [1.5]
HCO ⁺ $J=3 \rightarrow 2$	267.558	25.7	29	13.7 \pm 0.8	16.9 \pm 0.9	15.4 \pm 0.9
HCN $J=3 \rightarrow 2$	265.886	25.5	29	5.1 \pm 0.8	7.0 \pm 0.8	6.9 \pm 0.8
HNC $J=3 \rightarrow 2$	271.981	26.1	28	2.4 \pm 0.6	2.7 \pm 0.7	3.5 \pm 0.6
C ₂ H $J=3 \rightarrow 2$	262.251	25.2	29	7.9 \pm 0.7	11.1 \pm 0.7	11.0 \pm 0.6
H ₂ CO (3 ₁₃ \rightarrow 2 ₁₂)	211.211	32.1	35	4.0 \pm 0.6	2.6 \pm 0.6	< 1.6 [1.5]
H ₂ CO (3 ₀₃ \rightarrow 2 ₀₂)*	218.222	21.0	34	2.3 \pm 0.6	3.6 \pm 0.6	3.1 \pm 0.6
H ₂ CO (4 ₁₄ \rightarrow 3 ₁₃)	281.527	45.6	27	< 2.5 [1.7]	< 2.6 [1.6]	3.3 \pm 0.9
H ₂ CO (4 ₀₄ \rightarrow 3 ₀₃)*	290.623	34.9	27	< 3.1 [1.0]	3.7 \pm 1.0	3.6 \pm 1.0
H ₂ CO (4 ₁₃ \rightarrow 3 ₁₂)	300.837	47.9	26	4.0 \pm 1.1	< 3.5 [2.6]	4.0 \pm 1.1
CH ₃ CCH $J=12 \rightarrow 11$	205.081	64.0	36	5.1 \pm 0.6	4.3 \pm 0.6	4.2 \pm 0.6
CH ₃ CCH $J=13 \rightarrow 12$	222.167	74.6	33	2.5 \pm 0.7	3.4 \pm 0.7	2.5 \pm 0.7
CH ₃ CCH $J=14 \rightarrow 13$	239.252	86.1	31	< 1.9 [1.0]	2.2 \pm 0.6	2.1 \pm 0.6
CH ₃ CCH $J=15 \rightarrow 14$	256.337	98.4	30	< 2.2 [1.0]	< 2.2 [1.4]	2.3 \pm 0.7

Note. — Measured line intensities and their estimated uncertainties or the three- σ upper limits for the 20 identified transitions in the three pointings. For the upper limits, the value is three times the 1- σ uncertainty in the fitted intensity and the fitted intensity value is given in square brackets. The adopted linewidth for all measurements is 250 km s⁻¹ (see text); changing this value by factors of two in either direction does not significantly change the fitted line intensities or the quality of the fit. The errors are based on the statistical errors in the spectral data and do not include any uncertainty due to calibration. The hyperfine splitting in the CN and C₂H transitions is not accessible at Z-Spec’s resolution. The H₂CO lines marked with an * may be blended with other higher energy H₂CO transitions.

imply that the isotopologue distribution is slightly more concentrated than the main species.

3.2.2. CN and C₂H

We detect both the CN $J=2 \rightarrow 1$ and C₂H $J=3 \rightarrow 2$ transitions in all pointings. The primary energy levels of both of these molecules are split by hyperfine interactions, giving spectra with more structure than is accessible using Z-Spec. The intensities quoted in Table 3 are obtained by fitting a single Gaussian profile and thus represent the total integrated intensity for all transitions. These species have been detected before in M82 by Henkel et al. (1988) and Fuente et al. (2005), but the $J=3 \rightarrow 2$ transition of C₂H is a new detection. Neither of these authors quotes the intensity seen in all hyperfine components, making a direct comparison difficult. Our emphasis is on a study of physical conditions which, if it included these species, would require knowledge of the intensities of the hyperfine components. Therefore, we do not include the CN and C₂H in this analysis that follows.

3.2.3. HCO⁺, HCN and HNC

The $J=3 \rightarrow 2$ transitions of these molecules are strongly detected in all three pointings. The HCO⁺ and HCN transitions have been previously detected by Wild et al. (1992) however the only previous detection of HNC in M82 has been the $J=1 \rightarrow 0$ line by Huettmeister et al. (1995). Comparing the 12'' beam measurements from Wild et al. (1992) to ours suggest a beam scaling exponent of roughly -1 , consistent with

the continuum and CO values. We use our measurements and measurements of other transitions in the subsequent analysis.

3.2.4. CS

Three transitions of CS lie in the Z-Spec band and its simple ladder of rotational transitions make it an ideal candidate for study with our instrument. Unfortunately, the lines in our band are not very bright in M82 so we can only give upper limits for the $J=6 \rightarrow 5$ lines and the $J=5 \rightarrow 4$ lines in the NE and SW pointings. The transitions we detect have been seen before in M82 by Bayet et al. (2008) for the CEN pointing and Bayet et al. (2009) for the NE and SW pointings. Longer integration times should enable the first detections of the $J=6 \rightarrow 5$ lines, particularly in the CEN pointing where the fitted intensity is 2.7σ . As with HCO⁺, HCN and HNC, we combine our measurements with the other measured transitions for the analysis that follows.

3.2.5. H₂CO

We have identified five transitions of formaldehyde which are detected in at least one of the three pointings and four of which have not been detected previously. Two of these transitions may be blended with other higher energy H₂CO lines and our reported integrated intensity should be interpreted as the sum of the intensities of all of these blended lines. The feature at 218 GHz has been studied with the heterodyne receiver array HERA on the IRAM 30m telescope by Mühle et al. (2007). They detected three formaldehyde transitions

near our NE and SW pointings along with a possible detection of a methanol line in the NE pointing. In addition, they demonstrated the power of using formaldehyde lines to trace both temperature and density of the molecular gas. Higher-resolution followup of the lines we have identified would provide a powerful extension to their work.

3.2.6. CH_3CCH

Methyl acetylene has the largest number of atoms of any molecule detected outside our galaxy and several transitions have been seen previously in the SW lobe of M82 (Mauersberger et al. 1991). Our measurements in the NE and CEN pointings as well as all the measurements of the $J = 12 \rightarrow 11$ and $J = 15 \rightarrow 14$ transitions are new. We suspect that the $J = 15 \rightarrow 14$ transition may be contaminated with an unidentified feature that is causing the fitted flux in the SW pointing to be unrealistically high. This spectral feature is right at our three-sigma threshold and additional data are needed to precisely determine the line identifications.

4. ANALYSIS

4.1. Excitation and Radiative Transfer Modeling

We turn now to a study of the physical conditions in the dense gas, as probed with rotational transitions of HCN, HNC, HCO^+ and CS. To make useful inferences about the conditions in M82's molecular gas, modeling is required. The approach is to adopt basic input parameters such as total amount of gas in the beam (column density), gas density, temperature, and abundance of the species under consideration and then calculate the resulting line intensities. A grid of such calculations over ranges of input parameters can then provide a framework to interpret the observations. We note that the transitions we study have a range of critical densities ranging from 10^4 to 10^8 cm^{-3} .

We use the RADEX code (van der Tak et al. 2008) for our excitation and radiative transfer modeling. The primary inputs to RADEX are the choice of molecule, the kinetic temperature of the molecular gas T_{kin} , the density of molecular hydrogen n_{H_2} in cm^{-3} and the column density of the species N_{mol} in cm^{-2} . The radiative transfer calculation depends on $N_{\text{mol}}/\Delta v$, where Δv is the velocity width of the line. Z-Spec cannot measure the linewidth, so $\Delta v = 250 \text{ km s}^{-1}$ is used throughout the radiative transfer modeling to be consistent with the linewidth used for the spectral fits. RADEX does not assume local thermal equilibrium, but uses an escape probability formalism that connects the optical depth to the chance an emitted photon escapes the source cloud. Several different physical models for this escape probability have been derived; we use the expanding spherical shell model. However, the results are very insensitive to the choice of escape probability. Starting with an initial guess for the level population distribution, RADEX computes the optical depths of all the molecule's transitions, from which a new level population distribution can be calculated. This process iterates until a self-consistent solution is achieved such that the optical depth changes by less than a default tolerance from one iteration to the next. We use the collisional excitation rates calculated in Lique et al. (2006) and Lique & Spielfiedel (2007) for

the CS species and the rates from the online database outlined in Schöier et al. (2005) for the three remaining species.

4.2. Parameter Likelihood Estimation

Calculated line intensities are then compared to the intensity measurements of the species under consideration. An additional area filling factor parameter Φ_A must be included in the model because the clumps of gas producing the radiation do not in general fill the beam. Φ_A scales down the line intensities from RADEX so that they can be directly related to the measurements. When Φ_A is less than 1, N_{mol} represents the column density of an individual radiating clump while the product $\Phi_A N_{\text{mol}}$ is the beam-averaged column density, $\langle N_{\text{mol}} \rangle$.

The line-intensity measurements are inherently uncertain and the physical interpretation using models should reflect that. A Bayesian method for calculating likelihood distributions for various physical quantities of interest can be used to address this measurement uncertainty (Ward 2002; Ward et al. 2003 [hereafter W03]). The method constructs the probability distribution of obtaining the measurements with their associated errors given a set of physical parameters, assuming the measurements are independent and the errors are Gaussian distributed. Using a prior-probability density function for the range of physical parameters, the probability distribution of the measurements given the physical parameters can be inverted into a likelihood distribution for the physical parameters given the measurement results.

Bayes' Postulate says that the prior probability density function should be uniform for all cases in the absence of prior knowledge. The prior probability distributions used for this analysis are assumed to be logarithmically uniform in all model parameters. However, this prior probability is used to exclude certain non-physical situations relating to large column densities and small molecular hydrogen densities. Both constraints require knowledge of the molecular abundance ratio, $X_{\text{mol}} \equiv n_{\text{mol}}/n_{H_2}$. These constraints limit the total molecular mass contained in the telescope beam to less than the dynamical mass of the galaxy ($2.0 \times 10^9 M_\odot$) and limit the column length, equal to the column density divided by the number density, to less than the length of the bright molecular emission on the plane of the sky (see also W03). In addition, models with optical depths larger than 100 in any transition are excluded because very large optical depths are not appropriate for the species under consideration and RADEX is not accurate when the optical depth is this large.

A critical aspect of the analysis is the scaling of the published measurements of various transitions to a common beamsize. The limits of beam scaling are θ^0 for a source that fills the beam for all measurements, and θ^{-2} for a source that is always smaller than the beam. M82 is in an intermediate range with respect to the $25''$ – $35''$ Z-Spec beam; it is neither fully point-like nor beam-filling. Based on the CO and mm-wave continuum maps, we use an intermediate beam scaling of θ^{-1} , appropriate for the distribution which is to first order extended along the major-axis, but unresolved along the minor axis.

4.3. Multi-Species Model

Four of the species detected in this survey have the required radiative and collisional rate data available in an

Table 4
High-Dipole-Moment Species Measurements

Transition	Rest Freq. (GHz)	E_{upper} (K)	Obs. Beam (arcsec)	NE Flux (K km s ⁻¹)	CEN Flux (K km s ⁻¹)	SW Flux (K km s ⁻¹)	Refs
CS							
$J=1 \rightarrow 0$	48.991	2.4	36	...	16.2 ± 1.1	...	2
$J=2 \rightarrow 1$	97.981	7.1	25.1	9.4 ± 0.2	13.3 ± 0.3	8.9 ± 0.2	3, 4
$J=3 \rightarrow 2$	146.969	14.1	16.7	8.9 ± 0.1	11.2 ± 0.3	7.6 ± 1.7	3, 4, 5
$J=4 \rightarrow 3$	195.954	23.5	37.1	4.3 ± 0.8	4.4 ± 0.8	4.1 ± 0.8	1
$J=5 \rightarrow 4$	244.936	35.3	30.8	< 0.5	2.3 ± 0.5	< 0.5	1
$J=6 \rightarrow 5$	293.912	49.4	26.3	< 1.0	< 1.1	< 1.0	1
C ³⁴ S							
$J=3 \rightarrow 2$	144.617	13.9	17	$\sim 0.5 \pm 50\%$	0.6 ± 0.1	$\sim 0.4 \pm 50\%$	6
$J=4 \rightarrow 3$	192.818	23.1	37.1	< 0.8	< 0.8	< 0.8	1
$J=5 \rightarrow 4$	241.016	34.7	30.8	< 0.5	< 0.5	< 0.5	1
$J=6 \rightarrow 5$	289.209	48.6	26.3	< 1.0	< 1.1	< 1.0	1
HCO ⁺							
$J=1 \rightarrow 0$	89.189	4.3	23	35.0 ± 2.0	38.3 ± 2.0	37.2 ± 2.0	7
$J=3 \rightarrow 2$	267.558	25.7	28.6	13.7 ± 0.8	16.9 ± 0.9	15.4 ± 0.9	1
$J=4 \rightarrow 3$	356.734	42.8	14	23.6 ± 1.7	22.2 ± 1.7	22.6 ± 1.9	8
HCN							
$J=1 \rightarrow 0$	88.632	4.3	23	21.8 ± 2.0	18.5 ± 2.0	23.7 ± 2.0	7
$J=3 \rightarrow 2$	265.886	25.5	28.8	5.1 ± 0.8	7.0 ± 0.8	6.9 ± 0.8	1
$J=4 \rightarrow 3$	354.505	42.5	14	5.6 ± 0.6	9.0 ± 0.7	6.1 ± 0.4	8
HNC							
$J=1 \rightarrow 0$	90.664	4.4	25	10.7 ± 2.0	13.4 ± 0.8	12.3 ± 3.0	9
$J=3 \rightarrow 2$	271.981	26.1	28.2	2.4 ± 0.6	2.7 ± 0.7	3.5 ± 0.6	1

References. — (1) This Work; (2) Paglione et al. 1995; (3) Bayet et al. 2008; (4) Bayet et al. 2009; (5) Mauersberger & Henkel 1989; (6) Martín et al. 2009; (7) Nguyen-Q-Rieu et al. 1989; (8) Seaquist & Frayer 2000; (9) Huettemeister et al. 1995.

Note. — Fluxes and upper limits used in our multi-species radiative transfer likelihood analysis. In addition to the given statistical error, a 10% calibration error is added in quadrature to each measurements' uncertainty. An additional 10% error is added to the lines measured in beams smaller than 18'' and to the CS $J=1 \rightarrow 0$ line. The CS $J=1 \rightarrow 0$ line has only been measured for the CEN pointing and thus is not included for the likelihood analysis for the other pointings. The C³⁴S $J=3 \rightarrow 2$ has also only been measured in the CEN pointing; we estimate the flux in the other pointings based on the $J=3 \rightarrow 2$ line ratio between CS and C³⁴S in the CEN pointing and apply a 50% error to these estimates for the likelihood analysis. The C³⁴S upper limits are based on the uncertainty in the spectral fit for the main-species lines; the actual integrated intensity in the C³⁴S lines is well below the detection threshold of our data.

online database (Schöier et al. 2005) or in the literature (Lique et al. 2006; Lique & Spielfiedel 2007): HCO⁺, HCN, HNC and CS. The method described in W03 and outlined in the previous section was developed for analyzing 11 transitions of CO and ¹³CO and it can be applied to each of the four molecules above individually. However, for three of the four selected molecules, the number of detected transitions (see Table 4) is less than the four primary parameters of the radiative transfer model (T_{kin} , n_{H_2} , N_{mol} and Φ_A). CS and C³⁴S have had several transitions measured but with relatively low signal-to-noise which would lead to very broad constraints from the likelihood analysis.

Observations of these four species in star-forming regions within our Galaxy indicate good correspondence with both the spatial distributions and the line profiles (Brand et al. 2001; Nikolić et al. 2003). High spatial resolution maps of the Galactic circumnuclear disk (Christopher et al. 2005) and of the starburst galaxy NGC 253 (Knudsen et al. 2007) in HCO⁺ and HCN indicate strong similarity, in general, between the emission of these two molecules.

We thus construct a model in which all four species are characterized by a common kinetic temperature, molecular hydrogen density, molecular hydrogen column density (N_{H_2}) and filling factor. Each species is modeled with a individual abundance (X_{mol}). Extraction of the absolute abundances relative to H₂ is not possible with RADEX,

but it can constrain the relative abundances of the various species. In the following analysis, CS is chosen as the primary species and the model is parameterized by T_{kin} , n_{H_2} , N_{CS} , Φ_A , $X_{\text{HCO}^+}/X_{\text{CS}}$, $X_{\text{HCN}}/X_{\text{CS}}$, $X_{\text{HNC}}/X_{\text{CS}}$ and $X_{\text{C}^{34}\text{S}}/X_{\text{CS}}$.

The result of the likelihood analysis is a likelihood matrix with each point in the matrix characterized by a particular value of the four primary species parameters and three secondary species abundance ratios which are used to parameterize the model. As described in W03, likelihood distributions for a single parameter can be obtained by integrating the likelihood matrix along all the other dimensions. These distributions, seen in Figures 3 and 4, can be used to calculate both median values and confidence ranges for the seven parameters in our model (see Table 5). It is also possible to calculate likelihood distributions for parameters which are functions of model parameters, such as the gas pressure, $P = n_{\text{H}_2} \times T_{\text{kin}}$, and beam-averaged column density, $\langle N_{\text{CS}} \rangle = \Phi_A \times N_{\text{CS}}$. The beam-averaged column density can be used to calculate the total molecular mass in the beam by

$$M_{\text{beam}} = 1.5 \times m_{\text{H}_2} \times \frac{\pi D_{\text{beam}}^2}{4} \times \frac{\langle N_{\text{mol}} \rangle}{X_{\text{mol}}} \quad (4)$$

where m_{H_2} is the mass of a hydrogen molecule, D_{beam} is the diameter of the beam and the factor of 1.5 accounts for the additional mass of He and dust in the molecular clouds. Distributions for these parameters and their as-

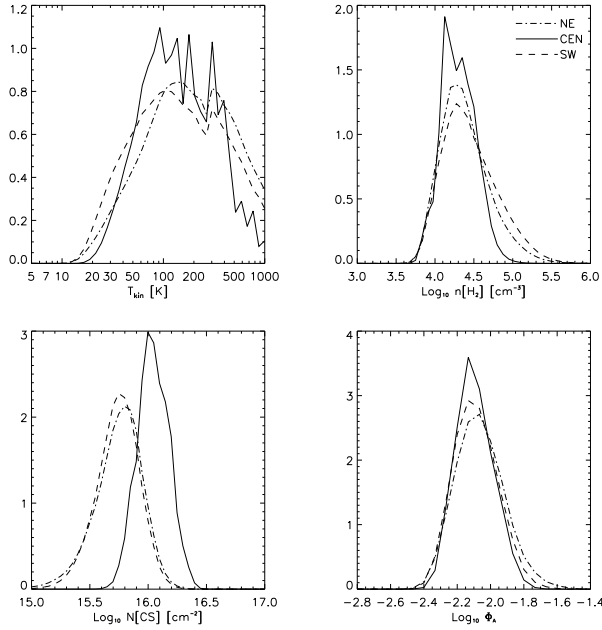


Figure 3. Likelihood distributions for the four primary species parameters, T_{kin} , n_{H_2} , N_{CS} and Φ_A , for the five-species radiative transfer likelihood analysis. All of the distributions have well defined peaks, indicating the parameters are well constrained by the measurements within the range of the RADEX simulation. The distributions for the three pointings are plotted in dash-dotted, solid and dashed lines for the NE, CEN and SW pointings, respectively. The distributions are normalized to have unit integral when integrated over the base-10 logarithm of the parameter value. The jaggedness seen in the T_{kin} distributions is caused by two factors: first, the spike seen in the distributions for all three pointings at 300 K is caused by patching together the two sets of collisional rates of CS from Lique et al. (2006) and Lique & Spielfiedel (2007). The former paper calculated the rates for 31 rotational levels for temperatures up to 300 K while the later produced rates for 38 rotational and 3 vibrational levels in a higher temperature range. The remaining jaggedness in the CEN pointing T_{kin} distribution probably comes from a numerical problem in RADEX where, for certain physical conditions, it fails to converge on a stable solution for the optical depth in the CS $J = 1 \rightarrow 0$ line. The NE and SW pointings' distributions do not show this effect because they do not have a CS $J = 1 \rightarrow 0$ measurement.

sociated two-dimensional distributions are shown in Figure 5.

The emitting regions containing these molecules are likely to be isolated cores of high-density gas. In that limit, we can estimate the velocity gradient inside the cores with a simple geometrical argument. The characteristic size of an individual core can be estimated by $S_{\text{core}} \approx (N_{\text{CS}}/X_{\text{CS}})/n_{\text{H}_2}$, which is simply the length defined by the ratio of the molecular hydrogen column and volume densities. This value can be used to estimate the number of cores in the beam by computing the ratio of the area of the emitting region in the beam over the size of a single core, $N_{\text{core}} \approx (\Phi_A \times D_{\text{beam}}^2)/S_{\text{core}}^2$. A reasonable approximation for isolated cores where $\Phi_A \ll 1$ is that the observed total line width Δv is split up equally among the individual cores. That implies that the velocity gradient in a single core is

$$\frac{dv}{dr} \approx \frac{\Delta v/N_{\text{core}}}{S_{\text{core}}} = \frac{\Delta v}{D_{\text{beam}}^2 X_{\text{CS}}} \times \frac{N_{\text{CS}}}{\Phi_A n_{\text{H}_2}}. \quad (5)$$

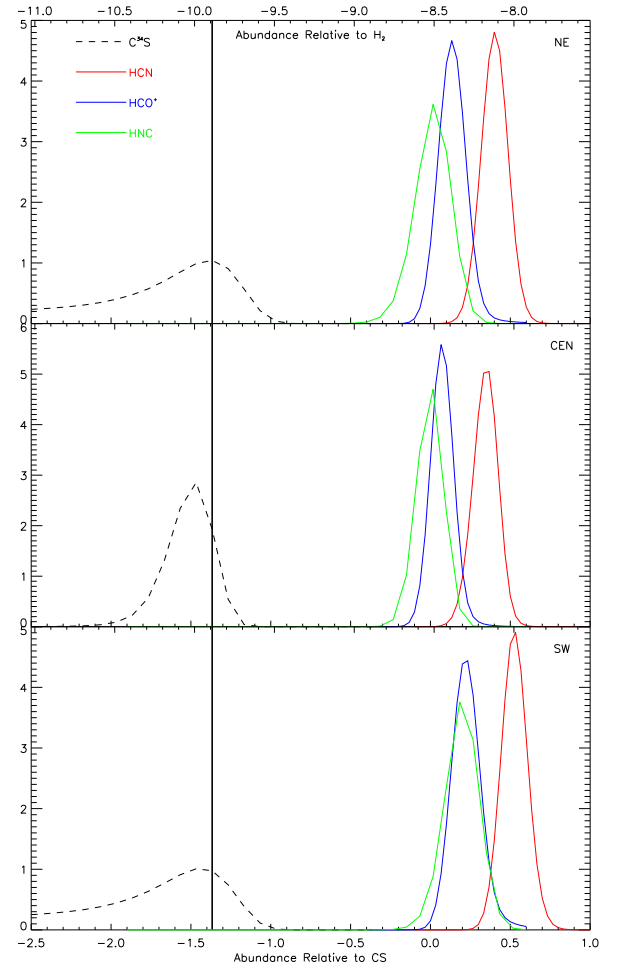


Figure 4. Likelihood distributions for the abundances of the secondary species, HCO^+ , HCN , HNC and C^{34}S in blue, red, green and dashed black, respectively, for the NE (top), CEN (middle) and SW (bottom) pointings. The thick vertical black line indicates the solar abundance of $^{34}\text{S}/^{32}\text{S} = 0.043$ that is assumed for calculating all other likelihood distributions. The bottom axis is labeled with the abundance relative to CS, which is the parameterization used in the model. The top axis shows the abundance relative to H_2 using the adopted value of $X_{\text{CS}} = 3 \times 10^{-9}$.

The distributions for the core velocity gradient are shown in Figure 5 along with two-dimensional projections of the three-dimensional distributions used for the calculation.

4.4. Molecular Abundances

The likelihood distributions of the HCO^+ , HCN , HNC and C^{34}S abundances relative to that of CS are shown in Figure 4. This represents the first statistically rigorous measurements of molecular abundances in M82. Average values for the entire starburst nucleus are presented in Table 6. As discussed in Section 4.2, the abundance of CS is used in the likelihood calculation to apply certain physical limits on the parameter space of the radiative transfer grid. We adopt the CS abundance X_{CS} of 3×10^{-9} calculated in Mauersberger & Henkel (1989). Their calculation is based on assuming optically thin CS emission and the CO intensity to H_2 column density conversion factor that is observed in the Milky Way. Changing the CS abundance by half an order of magnitude

Table 5
Multi-Species Modeling Results

Quantity	NE Pointing		CEN Pointing		SW Pointing	
	Median	Range	Median	Range	Median	Range
Primary Species Parameters						
T_{kin} (K)	160	58 - 470	130	56 - 320	130	44 - 410
n_{H_2} (cm^{-3})	$10^{4.3}$	$10^{4.0} - 10^{4.7}$	$10^{4.2}$	$10^{4.0} - 10^{4.5}$	$10^{4.4}$	$10^{4.1} - 10^{4.8}$
N_{CS} (cm^{-2})	$10^{15.7}$	$10^{15.5} - 10^{15.9}$	$10^{16.0}$	$10^{15.9} - 10^{16.2}$	$10^{15.7}$	$10^{15.5} - 10^{15.9}$
Φ_{A}	$10^{-2.1}$	$10^{-2.3} - 10^{-1.9}$	$10^{-2.1}$	$10^{-2.3} - 10^{-2.0}$	$10^{-2.1}$	$10^{-2.3} - 10^{-2.0}$
Secondary Species Relative Abundances						
$X_{\text{HCO}^+}/X_{\text{CS}}$	$10^{0.1}$	$10^{0.0} - 10^{0.2}$	$10^{0.06}$	$10^{-0.02} - 10^{0.13}$	$10^{0.2}$	$10^{0.1} - 10^{0.3}$
$X_{\text{HCN}}/X_{\text{CS}}$	$10^{0.4}$	$10^{0.3} - 10^{0.5}$	$10^{0.3}$	$10^{0.2} - 10^{0.4}$	$10^{0.5}$	$10^{0.4} - 10^{0.6}$
$X_{\text{HNC}}/X_{\text{CS}}$	$10^{0.0}$	$10^{-0.2} - 10^{0.1}$	$10^{0.0}$	$10^{-0.2} - 10^{0.1}$	$10^{0.2}$	$10^{0.0} - 10^{0.3}$
$X_{\text{C}^{34}\text{S}}/X_{\text{CS}}$	$10^{-1.7}$	$10^{-2.7} - 10^{-1.3}$	$10^{-1.6}$	$10^{-1.7} - 10^{-1.4}$	$10^{-1.8}$	$10^{-2.7} - 10^{-1.4}$
Projected Parameters						
Pressure (K cm^{-3})	$10^{6.6}$	$10^{6.3} - 10^{6.8}$	$10^{6.4}$	$10^{6.2} - 10^{6.6}$	$10^{6.5}$	$10^{6.3} - 10^{6.8}$
$\langle N_{\text{CS}} \rangle$ (cm^{-2})	$10^{13.6}$	$10^{13.5} - 10^{13.8}$	$10^{13.9}$	$10^{13.8} - 10^{14.0}$	$10^{13.6}$	$10^{13.4} - 10^{13.7}$
dv/dr ($\text{km s}^{-1} \text{ pc}^{-1}$)	1.9	0.6 - 4.4	4.5	3.0 - 7.2	1.6	0.5 - 4.1
Total Gas Mass in Beam (M_{\odot})	$10^{7.9}$	$10^{7.8} - 10^{8.1}$	$10^{8.2}$	$10^{8.1} - 10^{8.3}$	$10^{7.9}$	$10^{7.8} - 10^{8.0}$

Note. — Results obtained from the multiple species radiative transfer modeling of the lines of CS, HCO^+ , HCN, HNC and C^{34}S . The median and 68% (1σ) confidence ranges are obtained from the likelihood distributions shown in Figures 3 – 5.

Table 6
Molecular Abundance Ratios for M82

Species	CS	HCO^+	HCN	HNC	C^{34}S
$\log_{10}(X_{\text{mol}})$	-8.5	-8.4	-8.1	-8.5	-9.9

Note. — Abundance ratios (with respect to H_2) derived from the multiple species modeling results for the abundance of HCO^+ , HCN, HNC and C^{34}S relative to CS and the abundance for CS relative to H_2 from Mauersberger & Henkel (1989). The uncertainty in the four modeled abundances is ± 0.1 and is less than ± 0.5 for CS in logarithmic units.

either up or down does not affect the likelihood distributions for nearly all of the parameters; the molecular hydrogen density and kinetic temperature distributions shift down and up, respectively, with increasing CS abundance such that the distribution of gas pressure is relatively unchanged. The agreement between the measured and most-likely model, shown graphically in Figure 6 for $X_{\text{CS}} = 3 \times 10^{-9}$, is not significantly impacted by changing X_{CS} . Furthermore, while the likelihood distributions for the C^{34}S abundance show slight differences between the three pointings, we have little reason to suspect that this value would be much different from the solar isotopic abundance ratio of $^{34}\text{S}/^{32}\text{S} = 0.043$. Therefore, we impose this isotopic ratio for the other likelihood calculations.

Of course, changing the assumed CS abundance impacts the conversion from the relative abundance ratios to standard abundances relative to H_2 . Also, while the beam-averaged column density distribution does not change when using different values for the CS abundance, the conversion from $\langle N_{\text{CS}} \rangle$ to total mass is inversely proportional to the abundance (see equation 4). Of the three values of CS abundance we have used, the value from Mauersberger & Henkel (1989) seems to be the most reasonable; lowering it drives the total molecular mass too high and raising it increases the temperatures to extreme values.

Adopting the value $X_{\text{CS}} = 3 \times 10^{-9}$ allows for comparison of our abundance measurements to those found

in the literature. For the most part, M82 is assumed to have abundances similar to those found in regions of high-mass star formation in our Galaxy such as Sgr B2 or Orion. Wild et al. (1992) quote $X_{\text{HCO}^+} = 1 \times 10^{-8}$ and $X_{\text{HCN}} = 2 \times 10^{-8}$ which have also been used by other authors (Seaquist & Frayer (2000), for example). These are somewhat higher than what we measure though we agree that HCN is twice as abundant as HCO^+ . Huettemeister et al. (1995) use their measurements of HCN $J=1 \rightarrow 0$ and the CO intensity to H_2 column density conversion factor to calculate $X_{\text{HNC}} = 1.4 \times 10^{-10}$, assuming the HCN emission is optically thin. Our measurements of the HNC $J=3 \rightarrow 2$ contradict the optically-thin assumption and our models point to an abundance 1.5 orders of magnitude larger, roughly equal to the CS abundance.

4.5. Mass of Dense Gas

The total mass of molecular gas in the nuclear region can be estimated from the total mass in the beam measured for each of the three pointings by adopting a particular geometry for the central region. If the area of the nucleus is A_{n} and the area of overlap between our $30''$ beam and this nuclear area is A_{ol} , then the total mass in the nucleus can be calculated using

$$M_{\text{total}} = M_{\text{CEN}} + M_{\text{NE}} \left(\frac{A_{\text{n}} - A_{\text{ol}}}{2A_{\text{ol}}} \right) + M_{\text{SW}} \left(\frac{A_{\text{n}} - A_{\text{ol}}}{2A_{\text{ol}}} \right), \quad (6)$$

where M_{CEN} , M_{NE} and M_{SW} are the masses measured in the three pointings. This equation uses the mass surface density implied by M_{NE} and M_{SW} to account for the mass not covered on the left and right sides of the CEN pointing. If we adopt a rectangular nuclear geometry $50'' \times 15''$, as indicated by the CO $J=2 \rightarrow 1$ interferometer maps in Weiß et al. (2001), then the area scaling factor $(A_{\text{n}} - A_{\text{ol}})/2A_{\text{ol}} = 0.37$ and $M_{\text{total}} = 2.2 \pm 0.5 \times 10^8 M_{\odot}$ in the nuclear starburst. This value is comparable to the total mass traced in CO from both multi-line studies (W03:

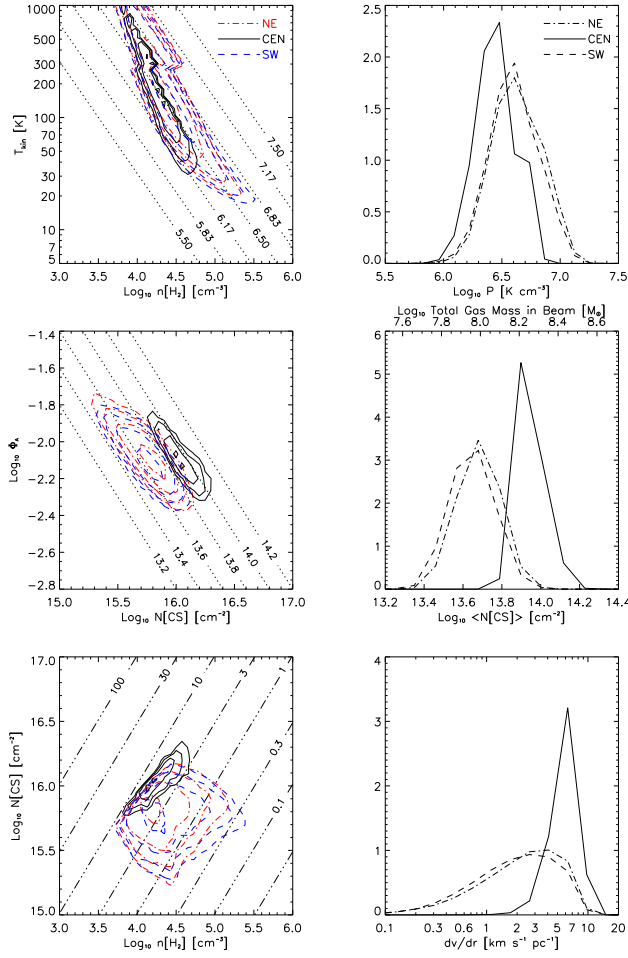


Figure 5. The plots in the left column show two-dimensional likelihood distributions for three pairs of primary species parameters while the right column plots show distributions for parameters that are projected from the corresponding 2D distributions. The three pointings, NE, CEN and SW, are indicated by red, black and blue contour lines in the 2D distributions and with dash-dotted, solid and dashed lines in the projected 1D distributions. The contour lines represent 10%, 20%, 40% and 80% of the peak of the 2D likelihood distributions. The top-left plot has dashed lines of constant pressure, labeled in units of $\log_{10} \text{K cm}^{-3}$; the T_{kin} versus n_{H_2} distributions are used to create the pressure distributions shown in the top-right plot. Dashed lines of constant beam-averaged column density in the left-middle Φ_A versus N_{CS} plot show how the $\langle N_{\text{CS}} \rangle$ distributions in the right-middle plot are obtained. The alternative axis in the beam-averaged column density plot shows the molecular mass in the beam assuming $X_{\text{CS}} = 3 \times 10^{-9}$. The bottom-left plot shows the N_{CS} versus n_{H_2} distributions; the diagonal dash-dot-dot-dot lines indicate constant velocity gradient in units of $\text{km s}^{-1} \text{pc}^{-1}$ at the most-likely value of Φ_A . The velocity gradient distributions shown in the bottom-right panel are computed from the three-dimensional distributions of N_{CS} , n_{H_2} and Φ_A .

$2.0 \times 10^8 M_{\odot}$ when corrected to $d = 3.86 \text{ Mpc}$) and via interferometric low- J CO and ^{13}CO imaging (Weiß et al. 2001).

HCN mass conversion— Since we measure a gas mass with a suite of transitions, we can provide a calibration of the HCN ‘ χ -factor,’ χ_{HCN} which converts HCN line luminosity (in temperature units) to mass of dense gas. Assuming that the source couples to the various beam

sizes as θ^1 , we find $\chi_{\text{HCN}, J=1}$ of 10–15, in agreement with the canonical value of 10 derived from virial considerations by Gao & Solomon (2004b,a). Since HCN is sub-thermally excited, χ_{HCN} using the $J = 3 \rightarrow 2$ transition is much higher: we find values of 36–65.

5. DISCUSSION

5.1. Physical Conditions, Relationship to CO-Traced Gas and Atomic Gas

Our likelihoods suggest temperatures between 50–500 K, broadly consistent with the warm components modeled by both W03 (up to $J = 6 \rightarrow 5$), and somewhat lower than the 400–800 K derived by Panuzzo et al. (2010) [hereafter P10] in considering all of the transitions up to $J = 13 \rightarrow 12$ as measured with *Herschel* SPIRE. Our results are also consistent with the 200 K inferred from the formaldehyde measurements Mühle et al. (2007). The relatively low precision with which we measure the temperature is estimated is not surprising, since these temperatures are generally higher than the upper level energies of the transitions we are studying (e.g. HCN $J = 3$: $T = 25 \text{ K}$), though we do note that our results do not support the presence of substantial amounts of gas at temperatures below $\sim 30 \text{ K}$, unless perhaps it is much lower density so as not to excite the transitions in our analysis. This means that the drop in line intensity with J (in temperature units) is due to sub-thermal excitation of the levels above $J = 1$, and the run of line intensity with J should thus provide a reliable density measurement. Indeed, our derived median densities are $1.5\text{--}3 \times 10^4 \text{ cm}^{-3}$, sub-critical for the transitions above 200 GHz.

Our derived densities are larger than those derived with CO studies: W03 find $600\text{--}6000 \text{ cm}^{-3}$ and P10 find $1000\text{--}13000$, though we do note in some cases W03 find densities poorly constrained on the high-density end. The product of temperature and density is the thermal pressure, and we find values ranging from $1\text{--}4 \times 10^6 \text{ K cm}^{-3}$, an order of magnitude higher than the pressure inferred by W03 ($0.5\text{--}4 \times 10^5 \text{ K cm}^{-3}$), but comparable to that derived by P10 using all of the CO transitions. Our high densities may reflect the fact that we are probing preferentially high-density cores, in approximate pressure equilibrium with the larger, more diffuse envelopes which produce the bulk of the CO. This should not be surprising since HCN, HNC, and CS are generally found in UV-shielded cores as their dissociation energies are less than that of CO, and they don’t have generally achieve sufficient column densities to self-shield. (See for example the PDR chemical models of Fuente et al. (2008) which show that HCN exists primarily within $A_V > 5$).

We compare our results with the studies of the photo-dissociated atomic gas. Kaufman et al. (1999) and Colbert et al. (1999) have applied a photo-dissociation region (PDR) model (updated from Wolfire et al. 1990; Tielens & Hollenbach 1985)⁵ to [C II] and [O I] fine-structure-line measurements from the Kuiper Airborne Observatory (KAO) and ISO Long-wavelength Spectrometer (LWS), respectively. PDR conditions are parametrized in terms of the density and UV

⁵ see also <http://dustem.astro.umd.edu/pdrt/index.html>

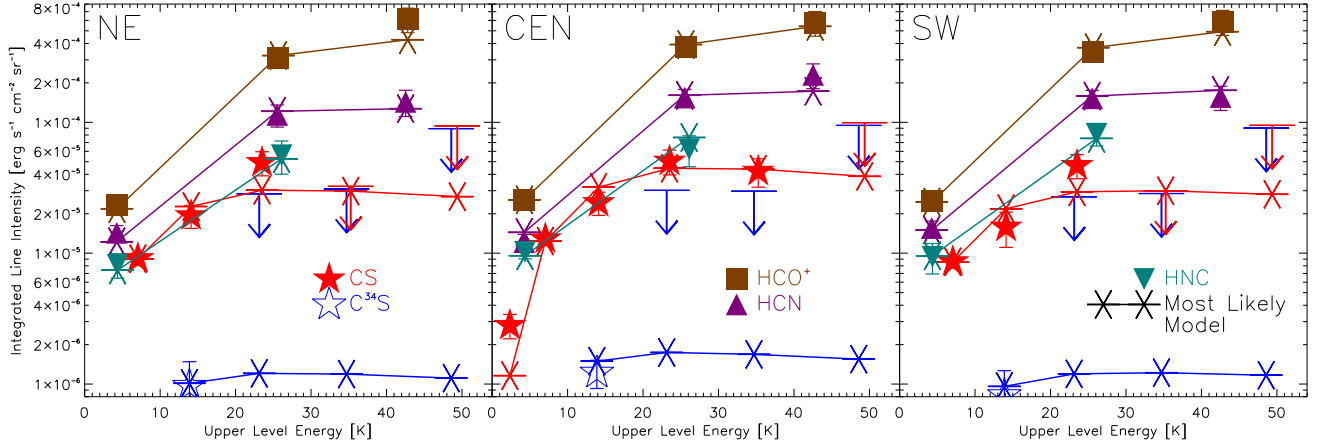


Figure 6. Measured and modeled spectral energy distributions for the five molecules of the multi-species radiative transfer likelihood analysis for the three pointings, NE (left), CEN (center) and SW (right). The measurements of CS, HCO⁺, HCN, HNC and C³⁴S, from Table 4 scaled to a common 30'' beam, are marked with red stars, brown squares, purple triangles, teal triangles and open blue stars, respectively. The error bars include both measurement and adopted calibration error, if any. Three-sigma upper limits are indicated with downward arrows using the same color scheme as the measurements. The most-likely model from the likelihood analysis is indicated by the six-pointed stars connected by lines, in colors to match the measurements.

field strength G_0 . Estimates for the M82 central starburst range from: 1) $n_{\text{H}_2}=10^4 \text{ cm}^{-3}$, $G_0=10^{3.5}$ (Kaufman et al. (1999), assuming the [C II] emission is uniformly distributed over its 55'' beam, so only a small fraction arises in the [O I]-emitting region), 2) $n_{\text{H}_2}=10^{2.7} \text{ cm}^{-3}$, $G_0=10^{2.5}$ (Kaufman et al. (1999), assuming that all the large-beam [C II] emission arises in the same region as the [O I]), and 3) $n_{\text{H}_2}=10^{3.3} \text{ cm}^{-3}$, $G_0=10^{2.8}$ (Colbert et al. (1999), using large-beam ISO fluxes, but removing a [C II] contribution from the ionized gas). These estimates form a locus in the n_{H_2} , G_0 plane, with the upper end of the density range becoming consistent with our density likelihood. The UV-illuminated surfaces of clouds might be expected to have somewhat lower density than the UV-shielded cores, and we note that with the modeled surface temperatures of $\sim 300 \text{ K}$, the PDR thermal pressures range from $10^{5.3}$ to $10^{6.5}$, broadly consistent with the values derived from the CO as well as our analysis.

However, the PDR models which fit the atomic line fluxes cannot explain the strength of the mid- J CO transitions. For the range of PDR conditions inferred from the atomic lines, the modeled CO $J=7 \rightarrow 6$ to [C II] intensity ratio is at most $\sim 1.7 \times 10^{-3}$ (at $n=10^4 \text{ cm}^{-3}$). The CO spectrum indeed peaks (in energy units) at $J=7 \rightarrow 6$ per the *Herschel* SPIRE measurements (P10). This transition carries a fraction 1.4–2.3% of the [C II], depending on whether the [C II] is resolved or unresolved in its 55'' beam, relative to the 43'' CO analysis region. Thus the CO emission in M82 exceeds the PDR predictions for the measured densities by an order of magnitude. Moreover, this is a lower limit—if the [C II] includes a contribution from ionized gas (as assumed by Colbert et al. 1999), then the inferred PDR line ratio is even larger, and less consistent with the model. Higher-density PDR models $n > 10^{4.5} \text{ cm}^{-3}$ can bring the mid- J CO to [C II] into agreement with the observations, but then the [O I] transition is over-predicted

relative to the observations by a factors of 3–10. Moreover, such high-densities for the PDR would be inconsistent with our measured density likelihood which excludes $n > 10^{4.5} \text{ cm}^{-3}$.

Empirically, the suite of [C II], [O I], and mid- J CO emission in M82 does not compare with the PDRs associated with Galactic star-formation regions. In M17, the bright mid- J CO and its widespread distribution with [C II] over several parsecs as viewed in the edge-on PDR led Stutzki et al. (1988); Harris et al. (1987) to a clumpy PDR interpretation. However, their data indicate that the CO $J=7 \rightarrow 6$ in this source only amounts to some $0.5\text{--}1 \times 10^{-3}$ relative to the [C II], much less than in M82. The Orion PDR is more extreme, with CO $J=7 \rightarrow 6$ some 8% of the [C II] (Schmidt-Burgk 1990; Stacey et al. 1993), but in this case the [O I] 63 μm line dominates the PDR line emission with $11\times$ the [C II] (see Herrmann et al. (1997)), so the CO $J=7 \rightarrow 6$ is $\sim 0.8\%$ of the atomic line emission. While the partitioning of energy between the atomic and warm molecular components in the Orion bar is thus similar to what we observe in M82, we stress again that the line ratio are not a good match, particularly the [O I] to [C II], which is only 1–1.5 in M82. The bright CO and [O I] in Orion is consistent with a clumpy PDR model which includes clumps with density as high as 10^7 cm^{-3} (Burton et al. (1990), see also (Koester et al. (1994); Meixner & Tielens (1993))). Such densities cannot be commonplace in M82 based on line ratios in the atomic gas, the CO analyses, and our analysis of the high-dipole-moment species which indicate typical densities less than $10^{4.5} \text{ cm}^{-3}$.

5.2. Heating of the Gas

The poor match to the Galactic PDRs and the inability of the PDR models to explain the powerful mid- J CO emission suggests that non-UV heating sources may be dominating the energetics of the molecular material in this starburst nucleus. X-rays can be a powerful source of energy input to the gas, producing luminous X-ray Disso-

ciation Regions (XDRs, Maloney et al. 1996). However, the hard X-ray luminosity of M82 is only $1.1 \times 10^6 L_\odot$ (Strickland & Heckman 2007), completely inadequate to power the observed CO emission. Moreover, multiple chemical / excitation studies show that the line emission from M82 is not consistent with X-rays being a dominant heating term. The XDR models of Meijerink & Spaans (2005) and Meijerink et al. (2007) predict more [O I] than is observed (Colbert et al. 1999) at our measured densities around 10^4 . Fuente et al. (2008) studied HOC^+ and HCO^+ in detail and showed that the HOC^+ emission is not spatially correlated with X-ray emission, and the line ratios among these species as well as CO^+ and CN are well-matched with PDR models with $n > 10^4 \text{ cm}^{-3}$ and $G_0 = 10^4$, similar to the values derived in analysis of the atomic lines. (They do not consider the total energy budget of the molecular gas, and do not discuss heating mechanisms.)

Similarly, Loenen et al. (2008) have considered XDR models and PDR models with and without extra bulk molecular heating and have predicted line ratios among the HCN, HCO^+ and HNC $J = 1 \rightarrow 0$ transitions. According to their models, the measurements for M82 (Table 4) are inconsistent with XDRs, as XDRs are predicted to have HNC comparable to or brighter than HCN. The line ratios are best fit with PDRs with $n \sim 10^{4.5}$ (their lowest density considered), but with additional bulk heating on the order of $3 \times 10^{-19} \text{ erg s}^{-1} \text{ cm}^{-3}$, $\sim 1 L_\odot / M_\odot$ input into the molecular material (they ascribe this to mechanical heating).

We thus look for other potential bulk heating sources other than X-rays. Suchkov et al. (1993) proposed that the elevated level of cosmic rays due to the supernova rate in M82 will heat the gas, and their derived cosmic ray enhancement factor relative to the Galaxy of ~ 500 has been confirmed by recent measurements of high-energy gamma-rays in M82 (VERITAS Collaboration et al. 2009). Bradford et al. (2003) showed that the energy input from a similar cosmic ray density is indeed well-matched to the total molecular gas cooling in NGC 253 as extrapolated from the CO transitions up to $J = 7 \rightarrow 6$ (where the CO emission appears to peak) (see also Hailey-Dunsheath et al. (2008)). Because the CO excitation and total cooling in M82 are similar (from W03, P10 fluxes), we conclude that cosmic rays are a plausible means of heating the gas.

Another important heating term for bulk molecular material is the dissipation of turbulence (Falgarone & Puget 1995; Mac Low 1999; Pan & Padoan 2009; see also: Bradford et al. 2005). The average heating per gram is given by dimensional analysis: $0.5 \times \sqrt{3} \sigma_v^3 / L$, where L is the driving scale for the turbulence and σ_v is the (1-D) RMS velocity spread on this size scale. Pan & Padoan (2009) conclude that turbulent dissipation with $\sigma_v \sim 2.5 \text{ km s}^{-1}$ on 0.1–1 pc scales is the dominant heating term on average in Galactic clouds (exceeding cosmic ray heating by factors of 3–4), and that it produces temperatures of 13–36 K in Galactic clouds with densities of 10^4 – 10^5 cm^{-3} . (For gas densities above 10^6 cm^{-3} , gas-grain cooling becomes dominant, and limits the increase in the gas temperature, as the dust energy balance is largely independent of the gas temperature.) A lower bound to the

total cooling per mass in M82 is given by the total CO luminosity in P10 ratioed to the mass derived by W03 using the mid- J lines: it is $\sim 0.1 L_\odot / M_\odot$. Achieving this via turbulent dissipation requires $\sigma_v \sim 5$ – 20 km s^{-1} on the same 0.1–1 pc scales. The velocity gradient implied by our radiative transfer analysis of 4 – $10 \text{ km s}^{-1} \text{ pc}^{-1}$ is a bit lower than this would suggest, but it becomes consistent if the turbulence is distributed on few-pc scales (e.g. $\sigma_v \sim 20 \text{ km s}^{-1}$, $L \sim 5 \text{ pc}$), as might be expected if it is produced by winds and supernova shocks from young star clusters.

5.3. Comparison with Expanding Shell Starburst Models

Our findings are largely consistent with the evolving starburst model of Yao (2009); Yao et al. (2006) in which the gas in the nucleus of M82 is a superposition of expanding spherical bubbles around stellar clusters. The bubble interiors are ionized gas ([H II] regions), and the shells are swept-up molecular gas, so the inside edges are photodissociation region (PDR) fronts. The PDR surfaces are responsible for most of the atomic line emission, and would agree with the Fuente et al. (2008) results. The PDR shell also generates most of the excited CO emission, though their model includes mechanical energy input from the shock due to the expansion, which may be a substantial term in the heating of the warm molecular gas.

Model intensities for the high-dipole moment species are not presented, preventing a detailed comparison with our data, but (not surprisingly) the total mass and physical conditions in their modeled shells are similar to what we find with our likelihood analysis. Their estimated gas mass of $2 \times 10^8 M_\odot$ from CO in the central 1 kpc along the major axis (nearly identical to our modeled $50'' \times 15''$ region) is comparable to our measured $2.2 \times 10^8 M_\odot$, and the shell density at the putative 3–10 Myr age is modeled to be 1 – $3 \times 10^4 \text{ cm}^{-3}$, similar to what we find. However, as Yao et al. note, there are some inconsistencies in their model: while they can reproduce all of the observed molecular and atomic line emission, the stellar luminosity which is required is only $\sim 5\%$ of the observed far-IR luminosity in the same region, potentially the result of assuming zero pressure for the ambient ISM which results in more mass swept up in the modeled shells than is physical.

5.4. Warm Star-Forming Gas

Regardless of the details, the Yao et al. model is representative of the likely physical situation: a new stellar cluster subjects the surrounding molecular gas to both UV photon and mechanical energy input which heats and compresses it, at least in the first 10 Myr after the starburst. The result is a molecular ISM that is demonstrably warmer than the Galactic cloud cores. Does this mean that the star formation is quenched? Fuente et al. (2008) compare line ratios of ions (HOC^+ , CO^+ to HCN) with their PDR chemistry model to estimate the total depth of the PDR (ions except HCO^+ quickly become less abundant with increasing A_V). Fitting the line ratios to two components, they find some $\sim 87\%$ of the molecular gas is in small clouds with $A_V \sim 5$ (but large enough to house HCN, HNC) with only $\sim 13\%$ in clouds with

$A_V \sim 50$ and conclude that in general the molecular gas is highly fragmented with clouds too small to form massive stars. Förster Schreiber et al. (2003) found that the star formation in M82 has occurred in two bursts, one in the center some 10 Myr ago and one in a circumnuclear ring ~ 5 Myr ago, and that each burst was self-quenching with a timescale of a few Myr due to mechanical energy input into the gas. The total mass of stars formed through both episodes is modeled at $2\text{--}5 \times 10^8 M_\odot$, depending on the low-mass part of the IMF (and cannot be more than $\sim 6 \times 10^8 M_\odot$, the total measured stellar mass in the system). The stellar mass formed in the last 10 Myr is thus comparable to or at most double the amount of dense molecular gas remaining, so unless the eventual star formation efficiency is limited to 30–50%, one may ask if the gas can be the raw material for another round of star formation.

If the material we trace is indeed forming stars, then the warm molecular medium is likely to impact the stellar initial mass function, increasing the fraction of high-mass stars by inhibiting the formation of low-mass stars. Theoretical studies of the IMF all involve scaling from a Jeans mass, the mass at which a cloud’s self-gravity overcomes its support forces (e.g. Larson 2005). The support can be either simple thermal pressure, or large-scale turbulent motions. In their recent analytical study, Hennebelle & Chabrier (2008) note that for typical ISM physical conditions and a reasonable prescription for the turbulence, the turbulent support is more important for the high-mass end of the spectrum, while the evolution of lower-mass condensations are governed by simple thermal support.

The thermal Jeans mass can be written as $M_J = 1.1 M_\odot (T/10\text{K})^{1.5} \rho_{19}^{-0.5}$ and yields $50 M_\odot$ for our median derived temperature (120 K) and density ($10^{4.2} \text{ cm}^{-3}$); ρ_{19} is the mass density in units of $10^{-19} \text{ g cm}^{-3}$. This may be indicating that the bulk of the material is indeed unlikely to participate meaningfully in any further star formation in its present condition. Of course, star formation will occur in the densest, coolest regions, but they would likely be in approximate pressure equilibrium with the bulk of the gas. If we consider the lowest temperatures allowed by our likelihood analysis: $T \sim 30$ K, together with the highest pressures: $\log P \sim 6.7$, the density is $n = 10^{5.2} \text{ cm}^{-3}$, and the Jeans mass is $M_J \sim 3 M_\odot$.⁶

A meaningful comparison with the Galaxy is hampered by the fact that our large-beam M82 observations are necessarily averaging over multiple star formation regions, and will include gas in outflows as well as collapsing protostars themselves. Our approach is to examine the material around the Galaxy’s most massive star formation sites, since they are likely the best Galactic examples of star formation on large scales. We consider the sample studied by Leurini et al. (2007) in the millimeter and centimeter-band methanol transitions which are used to derive accurate temperatures and densities. We

consider only the envelopes rather than the cores since the cores appear to be heated internally and are presumably already undergoing collapse, and in any case, the envelopes dominate the mass of these regions.

Leurini et al. (2007) find temperatures ranging from 11–36 K, and densities of $10^5\text{--}10^6 \text{ cm}^{-3}$. Thus even these massive star formation sites are cooler on average than the dense gas in M82. The lower temperature is not surprising; again, in dense regions the gas temperature will approach the dust temperature, which in the Galaxy ranges from 10–20 K (Paradis et al. 2009). While the inferred thermal pressures in these star forming envelopes are comparable to those we find in M82, the lower temperature and higher density corresponds to a smaller typical Jeans mass—values range from 0.3–2.8 M_\odot , less than the minimum $\sim 3 M_\odot$ derived above for M82.

More generally, the characteristic formed stellar mass scale M_* is seen to scale as T_{\min}^γ , where T_{\min} is the minimum temperature to which the gas can cool, and the exponent γ ranges from 1.7 (obtained in numerical experiments, Jappsen et al. 2005) to 3.35 (via an analytic treatment, Larson 1985). If we take the measured minimum of ~ 30 K versus a conservative 20 K in the warm Galactic regions, this scaling suggests a factor of at least 2–4 in M_* for M82 relative to the Galaxy. Clearly, accurate estimates require theoretical study and more detailed knowledge of the local conditions at the star formation sites, but if the gas we are tracing is indeed involved in star formation, then it likely produces a stellar IMF which is biased against low-mass stars relative to even the massive star formation sites in the Galaxy.

Such a scenario is of course consistent with the reports of low-mass-deficient stellar populations in M82 over the years (Rieke et al. 1980, 1993; Förster Schreiber et al. 2003). Moreover, an IMF biased against low-mass stars produces more luminosity per unit stellar mass than if the IMF is as observed in the Galaxy. Such a top-heavy or bottom-light IMF has been proposed to explain an apparent discrepancy between the observed stellar mass buildup and the energy release history in the first half of the Universe ($z > 1$) (Pérez-González et al. 2008; Davé 2008). Given that the typical star forming galaxy in this epoch is now believed to be similar to the local LIRGs and ULIRGs (Le Floch et al. 2005; Papovich et al. 2007), the conditions in M82 are likely more indicative of the historical average than those of the Galaxy.

6. CONCLUSIONS

We present a study of the dense molecular gas in the starburst nucleus of M82 based on 190–307 GHz spectra toward three positions obtained with the Z-Spec instrument. Z-Spec offers good sensitivity, accurate continuum measurement, and a uniform calibration for spectral lines across this band, and we report fluxes for some 20 molecular transitions, many new detections. The measurements of the $J = 3 \rightarrow 2$ transitions of HCO^+ , HCN, and HNC, and the $J = 4 \rightarrow 3$ and $J = 5 \rightarrow 4$ transitions of CS motivate an excitation and radiative transfer analysis in which all four species are simultaneously considered, incorporating all of their available published transitions. Our analysis constrains the physical conditions in the dense gas as well as the relative abundances among these species. We trace some $1.7\text{--}2.7 \times 10^8 M_\odot$ of gas with

⁶ We note for completeness that there is evidence for a (mass-independent) efficiency factor that relates the mass of a Jeans-unstable core to the mass of the actual star which forms from it, believed to be $\sim 1.4\text{--}2$ (Hennebelle & Chabrier 2008), meaning that the resulting stellar masses are somewhat smaller than the Jeans mass estimates.

$n_{\text{H}_2} \simeq 1\text{--}3 \times 10^4 \text{ cm}^{-3}$, and find that it is warm: likely above 50 K and potentially as high as 500 K, a range which exceeds the level temperature of the transitions studied. The mass and temperature are thus comparable to that found for the warm component in the mid- J CO studies, but the higher density implies a thermal pressure of $1.5\text{--}4 \times 10^6 \text{ K cm}^{-3}$, about an order of magnitude higher than inferred from the mid- J CO transitions.

In the framework of physical and chemical models, the line ratios among HCN, HCO^+ and HNC indicate that the molecular gas is subject to both UV photons as well as a bulk heating mechanism other than X-rays. A similar conclusion is reached in considering the direct observed cooling in the CO lines up to $J = 7 \rightarrow 6$. Cosmic ray heating and dissipation of mechanical energy from the new star clusters are both potential heating sources for the molecular ISM in M82. This feedback has rendered much of the molecular ISM in the nucleus sterile to further star formation. We briefly compare the dense molecular gas in M82 with star-forming sites in the Galaxy, concluding that if any of the material we are studying is involved in further star formation, then the increased heating likely biases the stellar IMF against low-mass stars, relative to the Galaxy. Such a scenario may be more indicative of the typical star formation environment in the Universe's history than the Galactic stellar IMF.

We are deeply grateful to the staff of the Caltech Submillimeter Observatory for their help in Z-Spec's commissioning and observing. We acknowledge Peter Ade and his group for some of our filters and Lionel Duband for the $^3\text{He}/^4\text{He}$ refrigerator in Z-Spec and are thankful for their help in the early integration of the instrument. Finally, we acknowledge the following grants and fellowships: NSF CSO grant (AST-0838261) for B. Naylor, NASA SARA grants NAGS-11911 and NAGS-12788, an NSF Career grant (AST-0239270) and a Research Corporation Award (RI0928) to J. Glenn, a Caltech Millikan and JPL Director's fellowships to C. M. Bradford, an NSF grant (AST-0807990) and an NRAO Jansky fellowship to J. Aguirre, and NASA GSRP fellowships to L. Earle and J. Kamenetzky.

REFERENCES

- Bayet, E., Aladro, R., Martín, S., Viti, S., & Martín-Pintado, J. 2009, *ApJ*, 707, 126
- Bayet, E., Lintott, C., Viti, S., Martín-Pintado, J., Martín, S., Williams, D. A., & Rawlings, J. M. C. 2008, *ApJ*, 685, L35
- Bradford, C. M., Nikola, T., Stacey, G. J., Bolatto, A. D., Jackson, J. M., Savage, M. L., Davidson, J. A., & Higdon, S. J. 2003, *ApJ*, 586, 891
- Bradford, C. M., Stacey, G. J., Nikola, T., Bolatto, A. D., Jackson, J. M., Savage, M. L., & Davidson, J. A. 2005, *ApJ*, 623, 866
- Bradford, C. M., et al. 2004, in Society of Photo-Optical Instrumentation Engineers (SPIE) Conference Series, Vol. 5498, Society of Photo-Optical Instrumentation Engineers (SPIE) Conference Series, ed. C. M. Bradford, P. A. R. Ade, J. E. Aguirre, J. H. Bock, M. Dragovan, L. Duband, L. Earle, J. Glenn, H. Matsuhara, B. J. Naylor, H. T. Nguyen, M. Yun, & J. Zmuidzinas, 257–+
- Bradford, C. M., et al. 2009, *ApJ*, 705, 112
- Brand, J., Cesaroni, R., Palla, F., & Molinari, S. 2001, *Astronomy and Astrophysics*, 370, 230
- Burton, M. G., Hollenbach, D. J., & Tielens, A. G. G. M. 1990, *ApJ*, 365, 620
- Carlstrom, J. E., & Kronberg, P. P. 1991, *Astrophysical Journal*, 366, 422
- Christopher, M. H., Scoville, N. Z., Stolovy, S. R., & Yun, M. S. 2005, *Astrophysical Journal*, 622, 346
- Colbert, J. W., et al. 1999, *Astrophysical Journal*, 511, 721
- Davé, R. 2008, *MNRAS*, 385, 147
- Earle, L. 2008, PhD thesis, University of Colorado at Boulder
- Earle, L., et al. 2006, in Society of Photo-Optical Instrumentation Engineers (SPIE) Conference Series, Vol. 6275, Society of Photo-Optical Instrumentation Engineers (SPIE) Conference Series
- Falgarone, E., & Puget, J. 1995, *A&A*, 293, 840
- Förster Schreiber, N. M., Genzel, R., Lutz, D., & Sternberg, A. 2003, *ApJ*, 599, 193
- Fuente, A., García-Burillo, S., Gerin, M., Teyssier, D., Usero, A., Rizzo, J. R., & de Vicente, P. 2005, *Astrophysical Journal Letters*, 619, L155
- Fuente, A., et al. 2008, *A&A*, 492, 675
- Gao, Y., & Solomon, P. M. 2004a, *ApJS*, 152, 63
- . 2004b, *ApJ*, 606, 271
- Glenn, J., et al. 2007, in Astronomical Society of the Pacific Conference Series, Vol. 375, From Z-Machines to ALMA: (Sub)Millimeter Spectroscopy of Galaxies, ed. A. J. Baker, J. Glenn, A. I. Harris, J. G. Mangum, & M. S. Yun, 63–+
- Hailey-Dunsheath, S., Nikola, T., Stacey, G. J., Oberst, T. E., Parshley, S. C., Bradford, C. M., Ade, P. A. R., & Tucker, C. E. 2008, *ApJ*, 689, L109
- Harris, A. I., Stutzki, J., Genzel, R., Lugten, J. B., Stacey, G. J., & Jaffe, D. T. 1987, *ApJ*, 322, L49
- Henkel, C., Schilke, P., & Mauersberger, R. 1988, *Astronomy and Astrophysics*, 201, L23
- Hennebelle, P., & Chabrier, G. 2008, *ApJ*, 684, 395
- Herrmann, F., Madden, S. C., Nikola, T., Poglitsch, A., Timmermann, R., Geis, N., Townes, C. H., & Stacey, G. J. 1997, *ApJ*, 481, 343
- Huettemeister, S., Henkel, C., Mauersberger, R., Brouillet, N., Wiklind, T., & Millar, T. J. 1995, *Astronomy and Astrophysics*, 295, 571
- Hughes, D. H., Gear, W. K., & Robson, E. I. 1994, *Monthly Notices of the Royal Astronomical Society*, 270, 641
- Jappsen, A., Klessen, R. S., Larson, R. B., Li, Y., & Mac Low, M. 2005, *A&A*, 435, 611
- Kaufman, M. J., Wolfire, M. G., Hollenbach, D. J., & Luhman, M. L. 1999, *ApJ*, 527, 795
- Knudsen, K. K., Walter, F., Weiss, A., Bolatto, A., Riechers, D. A., & Menten, K. 2007, *Astrophysical Journal*, 666, 156
- Koester, B., Stoerzer, H., Stutzki, J., & Sternberg, A. 1994, *A&A*, 284, 545
- Larson, R. B. 1985, *MNRAS*, 214, 379
- . 2005, *MNRAS*, 359, 211
- Le Floch, E., et al. 2005, *ApJ*, 632, 169
- Leeuw, L. L., & Robson, E. I. 2009, *AJ*, 137, 517
- Laurini, S., Schilke, P., Wyrowski, F., & Menten, K. M. 2007, *A&A*, 466, 215
- Lique, F., & Spieffiedel, A. 2007, *Astronomy and Astrophysics*, 462, 1179
- Lique, F., Spieffiedel, A., & Cernicharo, J. 2006, *Astronomy and Astrophysics*, 451, 1125
- Loenen, A. F., Spaans, M., Baan, W. A., & Meijerink, R. 2008, *A&A*, 488, L5
- Mac Low, M. 1999, *ApJ*, 524, 169
- Maloney, P. R., Hollenbach, D. J., & Tielens, A. G. G. M. 1996, *ApJ*, 466, 561
- Mao, R. Q., Henkel, C., Schulz, A., Zielinsky, M., Mauersberger, R., Störzer, H., Wilson, T. L., & Gensheimer, P. 2000, *Astronomy and Astrophysics*, 358, 433
- Martín, S., Martín-Pintado, J., & Mauersberger, R. 2009, *ApJ*, 694, 610
- Mauersberger, R., & Henkel, C. 1989, *Astronomy and Astrophysics*, 223, 79
- Mauersberger, R., Henkel, C., Walmsley, C. M., Sage, L. J., & Wiklind, T. 1991, *Astronomy and Astrophysics*, 247, 307
- Meijerink, R., & Spaans, M. 2005, *A&A*, 436, 397
- Meijerink, R., Spaans, M., & Israel, F. P. 2007, *A&A*, 461, 793
- Meixner, M., & Tielens, A. G. G. M. 1993, *ApJ*, 405, 216
- Morris, M., Palmer, P., Turner, B. E., & Zuckerman, B. 1974, *ApJ*, 191, 349
- Mühle, S., Seaquist, E. R., & Henkel, C. 2007, *ApJ*, 671, 1579
- Naylor, B. J., et al. 2003, in Society of Photo-Optical Instrumentation Engineers (SPIE) Conference Series, Vol. 4855, Society of Photo-Optical Instrumentation Engineers (SPIE) Conference Series, ed. T. G. Phillips & J. Zmuidzinas, 239–248
- Nguyen-Q-Rieu, Nakai, N., & Jackson, J. M. 1989, *Astronomy and Astrophysics*, 220, 57
- Nikolić, S., Johansson, L. E. B., & Harju, J. 2003, *Astronomy and Astrophysics*, 409, 941
- Paglionie, T. A. D., Jackson, J. M., Ishizuki, S., & Rieu, N. 1995, *AJ*, 109, 1716
- Pan, L., & Padoan, P. 2009, *ApJ*, 692, 594

- Panuzzo, P., et al. 2010, ArXiv e-prints
- Papovich, C., et al. 2007, *ApJ*, 668, 45
- Paradis, D., Bernard, J., & Mény, C. 2009, *A&A*, 506, 745
- Pérez-González, P. G., et al. 2008, *ApJ*, 675, 234
- Rieke, G. H., Lebofsky, M. J., Thompson, R. I., Low, F. J., & Tokunaga, A. T. 1980, *ApJ*, 238, 24
- Rieke, G. H., Loken, K., Rieke, M. J., & Tamblyn, P. 1993, *ApJ*, 412, 99
- Sakai, S., & Madore, B. F. 1999, *Astrophysical Journal*, 526, 599
- Sanders, D. B., Mazzarella, J. M., Kim, D.-C., Surace, J. A., & Soifer, B. T. 2003, *Astronomical Journal*, 126, 1607
- Satyapal, S., Watson, D. M., Pipher, J. L., Forrest, W. J., Greenhouse, M. A., Smith, H. A., Fischer, J., & Woodward, C. E. 1997, *ApJ*, 483, 148
- Schmidt-Burgk, J. 1990, in *Astrophysics and Space Science Library*, Vol. 158, *Submillimetre Astronomy*, ed. G. D. Watt & A. S. Webster, 11–12
- Schöier, F. L., van der Tak, F. F. S., van Dishoeck, E. F., & Black, J. H. 2005, *Astronomy and Astrophysics*, 432, 369
- Seaquist, E. R., & Frayer, D. T. 2000, *Astrophysical Journal*, 540, 765
- Seaquist, E. R., Lee, S. W., & Moriarty-Schieven, G. H. 2006, *ApJ*, 638, 148
- Solomon, P. M., Downes, D., & Radford, S. J. E. 1992, *Astrophysical Journal Letters*, 398, L29
- Stacey, G. J., Jaffe, D. T., Geis, N., Grenzel, R., Harris, A. I., Poglitsch, A., Stutzki, J., & Townes, C. H. 1993, *ApJ*, 404, 219
- Strickland, D. K., & Heckman, T. M. 2007, *ApJ*, 658, 258
- Stutzki, J., Stacey, G. J., Genzel, R., Harris, A. I., Jaffe, D. T., & Lugten, J. B. 1988, *ApJ*, 332, 379
- Suchkov, A., Allen, R. J., & Heckman, T. M. 1993, *ApJ*, 413, 542
- Thuma, G., Neininger, N., Klein, U., & Wielebinski, R. 2000, *Astronomy and Astrophysics*, 358, 65
- Tielens, A. G. G. M., & Hollenbach, D. 1985, *ApJ*, 291, 722
- Turner, B. E., Zuckerman, B., Palmer, P., & Morris, M. 1973, *ApJ*, 186, 123
- van der Tak, F. F. S., Aalto, S., & Meijerink, R. 2008, *A&A*, 477, L5
- VERITAS Collaboration et al. 2009, *Nature*, 462, 770
- Ward, J. S. 2002, PhD thesis, California Institute of Technology
- Ward, J. S., Zmuidzinas, J., Harris, A. I., & Isaak, K. G. 2003, *Astrophysical Journal*, 587, 171
- Weiß, A., Neininger, N., Hüttemeister, S., & Klein, U. 2001, *Astronomy and Astrophysics*, 365, 571
- Weiß, A., Walter, F., & Scoville, N. Z. 2005, *A&A*, 438, 533
- Wild, W., Harris, A. I., Eckart, A., Genzel, R., Graf, U. U., Jackson, J. M., Russell, A. P. G., & Stutzki, J. 1992, *Astronomy and Astrophysics*, 265, 447
- Wolfire, M. G., Tielens, A. G. G. M., & Hollenbach, D. 1990, *ApJ*, 358, 116
- Wu, J., Evans, II, N. J., Gao, Y., Solomon, P. M., Shirley, Y. L., & Vanden Bout, P. A. 2005, *ApJ*, 635, L173
- Yao, L. 2009, *ApJ*, 705, 766
- Yao, L., Bell, T. A., Viti, S., Yates, J. A., & Seaquist, E. R. 2006, *ApJ*, 636, 881